SCIPEDIA Revista Internacional de Métodos Numéricos para Cálculo y Diseño en Ingeniería

RIMNI Revista Internacional Métodos numéricos para cálculo y diseño en ingeniería

Effects of Radar Absorption Materials Application on Stealth Performance of Inlet Based on Risk Theory

Shuang Liu[1,*], Zhiyin Guo[2,3] and Lihai Chen[4]

[1]School of Aero-Engine, Zhengzhou University of Aeronautics, Zhengzhou, 450046, China

[2]School of Humanities and Law, Zhengzhou University of Aeronautics, Zhengzhou, 450046, China

[3]Social Science Department, University of Gdańsk, Gdańsk, 80-309, Poland

[4]Department of Thermal Engineering, Hebei Petroleum University of Technology, Chengde, 067000, China

*Corresponding Author: Shuang Liu. Email: liushuang@zua.edu.cn

ABSTRACT

One significant technical measure to reduce the forward radar cross section (RCS) of the aircraft was to design the inlet into an S-shape. Additionally, the application of radar-absorbing material (RAM) can further decrease the RCS of the air intake which approach enhances the stealth capabilities of the aircraft. Nevertheless, the use of RAM will simultaneously increase the inherent weight of the air intake. The electromagnetic scattering characteristics of S-shaped inlets without RAM coating and seven coating schemes are calculated by numerical simulation. The risk theory was employed to assess the impact of the coating RAM on the radar cross-section. The simulation results indicate that coating RAM can further reduce the forward average RCS value. Compared to the full coating scheme the S-shaped inlets with RAM on the intake region can achieve 90% of the RCS reduction effect and cut down approximately forty percent of the coating.

OPEN ACCESS

Accepted: 27/09/2024

Submited: 24/07/2024

DOI
110.23967/
j.rimni.2024.10.56526

Keywords: S-shaped inlet; radar cross section; coating scheme; risk theory

1 Introduction

The primary function of the inlet of the aero-engine is to capture, supercharge, and rectify the airflow. The design features and operational characteristics of the inlet play a critical role in the efficiency and operational envelope of the aero-engine [1]. Furthermore, the inlet serves as one of the principal sources of the forward electromagnetic scattering of the aircraft. As a results, the advanced air inlets are required not only to enhance their aerodynamic performance but also to improve their stealth capabilities [2,3].

Extensive research has been undertaken by scholars both domestically and internationally on the internal flow field characteristics of S-shaped pipes utilized in aero-engines. Asghar et al. [4] evaluated the internal performance of S-duct diffusers with varying offset-to-length ratios using both numerical simulation and experimental methods. As the offset-to-length ratio increased, there is a

decrease in static pressure recovery and an increase in total pressure loss. Mclelland et al. [5] provided the inaugural quantitative assessment of the impact of inlet boundary layer thickness and asymmetry on the swirl distortion at the exit of the S-shaped intake. The results indicate that the peak swirl intensity increases by 40% when the boundary layer is seven times thicker than the reference case. Although the dominant fluctuations in the flow arise at a frequency 50% lower, the unsteady modes of the S-duct remain. Migliorini et al. [6] investigated the influence of the inlet boundary layer on the unsteady aerodynamics of the S-duct inlet using time-resolved particle image velocimetry at the aerodynamic interface plane. The results indicate that an increase in the boundary layer thickness at the intake inlet augments the flow unsteadiness on the swirl angle by up to 40% relative to the baseline case, and proposed guidelines for the integration between the inlet and the engine across a broad spectrum of potential inlet operating conditions. Ning et al. [7] conducted a numerical simulation on S-shaped inlet ingesting a substantial amount of freestream boundary layer. The results demonstrate that the total pressure recovery coefficient has decreased by 0.04 as a consequence of the boundary layer ingestion. As the outlet Mach number increases, the total pressure recovery coefficient initially rises and then declines, while it decreases monotonously in an S-shaped inlet without boundary layer ingestion. Song et al. [8] tested a subsonic S-shaped inlet with eight configurations of curved-edge plate-type distortion generators designed to generate a complex distorted flow field downstream. The experimental results revealed that the radial index decreased by an average of 62%. The overall swirl intensity index decays by 37% to 70% only for bilaterally symmetrical modes while remaining approximately constant for bilaterally asymmetrical modes. Gil-Prieto et al. [9] employed time-resolved particle image velocimetry to ascertain the three-component velocity field at the outlet plane of a double S-duct inlet across a spectrum of Mach numbers. The investigation yielded a unique time-resolved dataset of synchronous velocity measurements with superior spatial resolution, thereby facilitating the analysis of unsteady flows at the exit of intricate aero-engine intakes. In the context of diffusing S-duct design, Gan et al. [10] introduced a modified shear stress transport turbulence model. When compared to the original design, the optimal duct design demonstrated a reduction in the flow distortion coefficient by 16.3% and an increase in the total pressure recovery factor by 1.1% under on-design conditions. This highlights the effectiveness of the modifications in enhancing the performance of the duct.

Research on the electromagnetic scattering characteristics of S-shaped pipes used in aero-engines has also been extensive. Shi et al. [11] studied the characteristics of radar cross section (RCS) of serpentine inlets at different azimuths, attack angles, and terminators. While Zhang et al. [12] studied the design parameter such as the influence of the centerline and area distributions on stealth performance. The results show that inlet stealth characteristics are more influenced by the centerline distribution than the area distribution. Wang et al. [13] carried out a numerical simulation to analysis the influence of absorbing materials with different electrical parameters on the RCS of the inlet. Gao et al. [14] studied the influence of coating radar absorbing material radar absorbing material (RAM) at different locations of double S-shaped nozzles on the RCS reduction. The research shows applying RAM at specific positions could optimize RCS reduction while minimizing material usage. He et al. [15] comprehensively optimized the aerodynamic characteristics and electromagnetic scattering characteristics for the serpentine nozzle using triangular outlets, achieving a 38.74% decrease in the objective function, an 83.33% reduction in RCS, and a 0.31% increase in total pressure recovery coefficient. Zhou et al. [16] developed a mixed design approach to reduce aircraft RCS and suppress infrared signatures while accounting for the influence of air inlet factors. Their approach effectively reduced the mean and tail RCS indices of the optimized aircraft model using physical optics and diffraction theory. Li et al. [17] proposed a gradient-based aerodynamic and

stealth optimization design method for flying wing aircraft that integrates the Free-Form Deformation approach, Radial Basis Function algorithm, Computational Fluid Dynamics, Physical Optics, and the Sequential Quadratic Programming algorithm. The optimization results show that the gradient-based aero-stealth optimization design method can handle multidisciplinary optimization problems involving a1 large number of design variables and also could rapidly and efficiently obtain the shape that meets the requirements of aerodynamic and stealth performances. Chen et al. [18] combined the Characteristic Basis Function Method (CBFM), Multilevel Fast Multipole Algorithm (MLFMA), Interpolation Decomposition(ID) algorithm and parallel technology to simulate the monostatic RCS of engine exhaust systems. The simulation results are in good agreement with the measured results, which demonstrates the accuracy of the algorithm.

Despite the wealth of research on the flow and electromagnetic scattering characteristics of S-shaped inlets, limited studies have examined the electromagnetic scattering characteristics of S-shaped inlets coated with RAM, particularly in relation to the trade-offs analyzed through risk management theory. To address this gap, this study designs seven different coating schemes for S-shaped inlets and simulates the corresponding RCS reduction effects.

2 Computation Scheme

2.1 Calculation Method

The Method of Moments (MoM) accelerated by MLFMA is used to calculate the RCS of the inlets. It's an efficient numerical solution for electromagnetic scattering and radiation problems [12].

The MoM discretizes the continuous electromagnetic field into a linear combination of basis functions and testing functions, transforming the differential or integral form of Maxwell's equations into an algebraic form of linear equations. These basis functions and testing functions are usually chosen to be simple geometric shapes, such as rectangles or triangles, for ease of computation. The MLFMM for acceleration is adopted to solve the large-scale linear equations generated by MoM. In MLFMM, each cubic grid is assigned a multipole expansion and a local expansion. The multipole expansion is used to describe the influence of the sources inside the cube on the outside, while the local expansion is used to describe the influence of the external sources on the inside of the cube. In this way, MLFMM can quickly and accurately calculate the scattering and radiation of the electromagnetic field [19,20].

Additionally, the impedance boundary condition is incorporated into the MoM algorithm to compute the electromagnetic scattering characteristics of cavities coated with RAM. The boundary condition is primarily applicable to non-ideal conductor surfaces and conductor surfaces coated with thin dielectric layers, relating the tangential component of the electromagnetic field on the target surface to a constant in a simplified form.

2.2 Risk Theory

Risk management theory, initially developed as an economic theory, involves the application of scientific methods and tools to analyze risk factors that may influence the achievement of objectives. The theory aims to systematically avoid or mitigate potential losses through activities such as planning, organizing, and controlling, based on the likelihood and impact of various risk factors. Risk probability estimation can be approached in two ways: the objective probability estimation method, which relies on historical statistical data to determine the probability distribution of risks, and the subjective probability estimation method, which is based on expert judgment. The goal of risk

measurement is to assign relevant values or rankings to these risks. Cardinal scales are utilized as they not only differentiate between various risks but also quantify the magnitude of their differences [21].

The risk management theory is used to assess the benefits between RCS reduction after the use of the absorbent material and the weight of the absorbent material itself. The following parameter δ characterizes the risk:

$$\delta = \left| \frac{RD}{A} \right| \tag{1}$$

$$RD = \frac{\sigma_n - \sigma_0}{\sigma_0} \times 100\% \tag{2}$$

where, A refers to the coating area; RD (reduction data) refers to the RCS reduction effect; σ_0 refers to the average RCS of the inlet without RAM coated; σ_n refers to the average RCS of the inlet with RAM coated.

2.3 Designed Coating Scheme

Fig. 1 shows the regional division diagram of the S-shaped inlet. The inlet is divided into 5 sections according to the axial distance. Table 1 shows the different coating program designed in this paper. Case 0 is the original model without RAM coating. Case 7 is the model with RAM coated on the entire inlet. Cases 1–3 are the models with RAM coated on the two non-adjacent parts of the wall surfaces. Cases 4–6 are the models with RAM coated on the three adjacent parts of the wall surfaces. The coating area ratio is determined by comparing with Case 7 which has a reference area ratio of one. The electrical properties of RAM used are as follows: $\mu_r = 1.0, \varepsilon_r = 6.11 - j0.78$. The thickness of RAM used is 0.006 m.

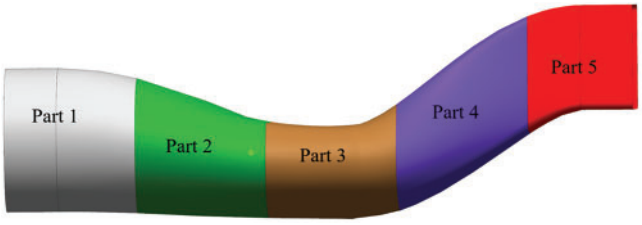

Figure 1: The regional division diagram

Table 1: The designed RAM coating scheme

	Part 1	Part 2	Part 3	Part 4	Part 5	Coating area
Case 0	○	○	○	○	○	0
Case 1	○	○	●	○	●	0.4035
Case 2	○	●	○	●	○	0.3807
Case 3	●	○	○	●	○	0.4331
Case 4	●	●	●	○	○	0.5986
Case 5	○	●	●	●	○	0.6504
Case 6	○	○	●	●	●	0.6187

(Continued)

Table 1 (continued)

	Part 1	Part 2	Part 3	Part 4	Part 5	Coating area
Case 7	•	•	•	•	•	1

3 Presentation of Results

3.1 Setting of Calculation Conditions

Fig. 2 shows the detection angle settings diagram. The detection angle ranges from −30° to 30° in the pitch plane and 0° to 30° in the yaw plane, with increments of 1°. The incident electromagnetic wave has a frequency of 10 GHz.

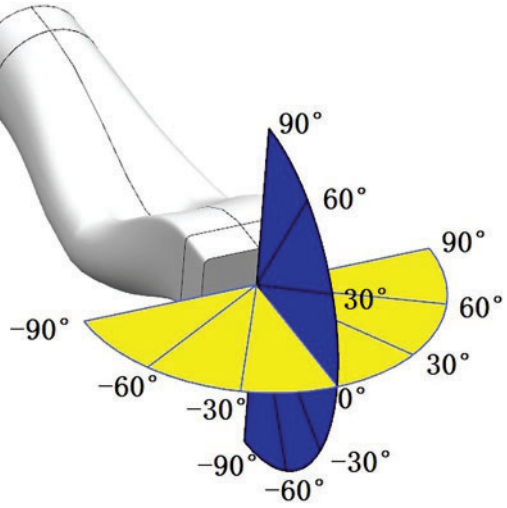

Figure 2: The detection angle setting diagram

3.2 Analysis of Coating Position

Fig. 3 presents the RCS curves of the S-shaped inlet under horizontal polarization in the pitch plane. The figure illustrates that the application of RAM on the inlet surface can effectively reduce the RCS across a majority of the detection angle range. However, the influence of RAM on the angular distribution pattern of the RCS is relatively minor. Different coating schemes yield similar angular distributions with the primary difference observed in the RCS amplitude when the detection angle range lies between −30° and −10°. Within this range, Case 4 exhibits the lowest RCS. The RCS of Cases 2 and 3 is higher than in Case 1, primarily due to the RAM coating at the intake part of the inlet, which directly reduces the amount of incident electromagnetic wave energy entering the cavity at larger detection angles. Cases 4–6 demonstrate a greater reduction effect than Cases 1–3 primarily attributed to the increased coating area on the wall. At a detection angle of approximately −10°, the RCS amplitudes of different coating schemes exhibit significant variation. When the detection angle range is between −10° and 0°, all coating schemes with the exception of Case 1 display a substantial RCS reduction effect. Within this detection angle range, the primary irradiation areas of incident electromagnetic waves are the non-RAM-coated Parts 3 and 4 of the inlet. The angular distribution

of RCS is similar across all cases from 0° to 10°. When the detection angle range is between 20° and 30°, Cases 1 and 4 yield the most significant RCS reduction, primarily because Parts 4 and 5, which are not coated with RAM, are directly irradiated by the incident electromagnetic wave.

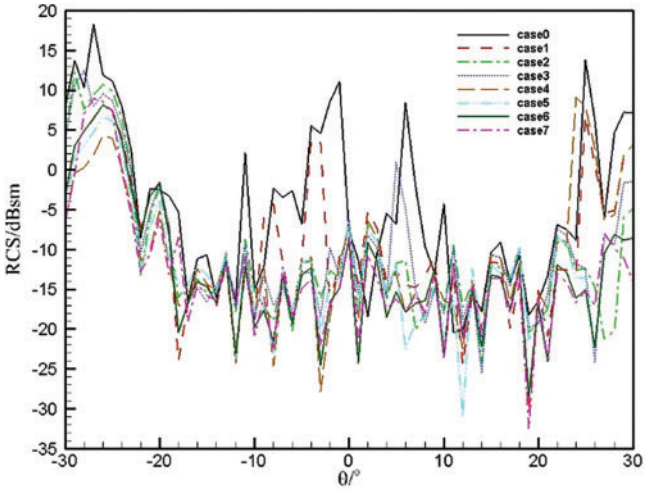

Figure 3: RCS curves of the S-shaped inlet in the horizontal polarization in the pitch plane

Fig. 4 presents the RCS curves for an S-shaped inlet under the vertical polarization in the pitch plane. The RCS curves across various cases exhibit a high degree of similarity. Within the detection angle range of −30° to 0°, the RCS angular distribution curves across different cases closely align, although the RCS amplitude is influenced by the application of RAM coated at various sections of the inlet. As the detection angle nears −4°, the RCS angular distributions for Cases 1 and 4 closely resemble that of Case 0. Despite the variations in coating schemes, the RCS angular distributions remain similar. Notably, Cases 6 and 7 demonstrate superior reduction effects compared to other coating schemes across a broader detection angle range. The amplitude of the RCS is primarily influenced by the differences in the coated sections, a characteristic more pronounced in vertical polarization compared to horizontal polarization. This is attributable to the polarization properties of the RAM and the geometric configuration of the S-shaped inlet. These findings underscore the critical role of RAM placement and polarization in optimizing RCS performance.

Fig. 5 presents the induced current distribution at $\theta = -6^{\circ}$ in the horizontal polarization in the pitch plane. In the coating schemes of Case 0, Case 2, and Case 4, regions of high-density induced current are observed on the upper wall of Part 5 and the lower wall of Part 3. Additionally, a region of medium-density induced current is present on the lower wall of Parts 1 and 2 in Case 2 and Case 3. These schemes effectively diminish the area of high-density induced current distribution, while exerting minimal impact on the distribution position. This observation underscores the potential of strategic RAM placement in managing induced current density and distribution within the inlet.

Fig. 6 presents the induced current distribution at $\theta = 20^{\circ}$ in vertical polarization. The figure illustrates that in the Case 0 scheme, Part 3 exhibits a region of high-density induced current on its lower wall. Notably, both the density and the area of this region decrease in the coating scheme which leading to a reduction in the medium-density region. The phenomenon can be primarily attributed to the fact that Part 3 is the focal point of the incident radar wave, where the incidence angle is relatively large. The observation underscores the influence of the incident radar wave's concentration and incidence angle on the induced current density within the inlet.

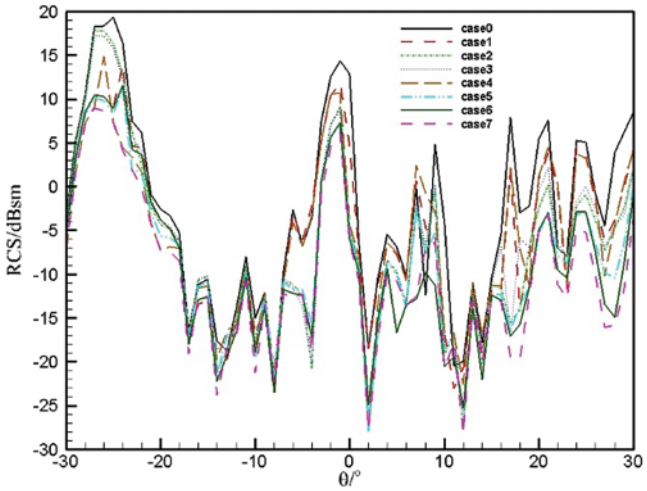

Figure 4: RCS curves of the S-shaped inlet in the vertical polarization in the pitch plane

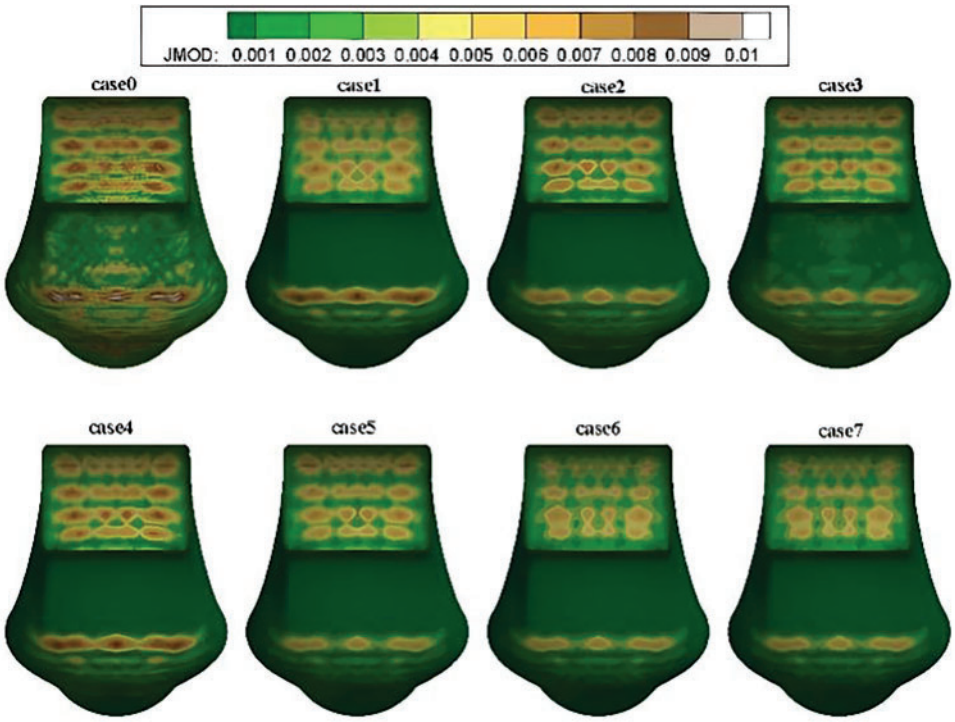

Figure 5: Induced current distribution at $\theta = -6^{\circ}$ in the horizontal polarization (unit: mA/m^2)

Fig. 7 shows the RCS curves of the S-shaped inlet under the horizontal polarization in the yaw plane. When the detection angle lies between 0° and 5°, the RCS angular distribution of the S-shaped inlet with RAM coating exhibits a distinct pattern compared to that without RAM coating. Concurrently, the RCS reduction is more pronounced with the RAM coating. Within other detection angle ranges, the RCS angular distribution and the RCS itself bear a resemblance to those observed on the yaw detection surface which can be primarily attributed to the relatively small area of the inner

wall of the intake port. The inner wall of the intake port can be directly irradiated by the incident electromagnetic wave.

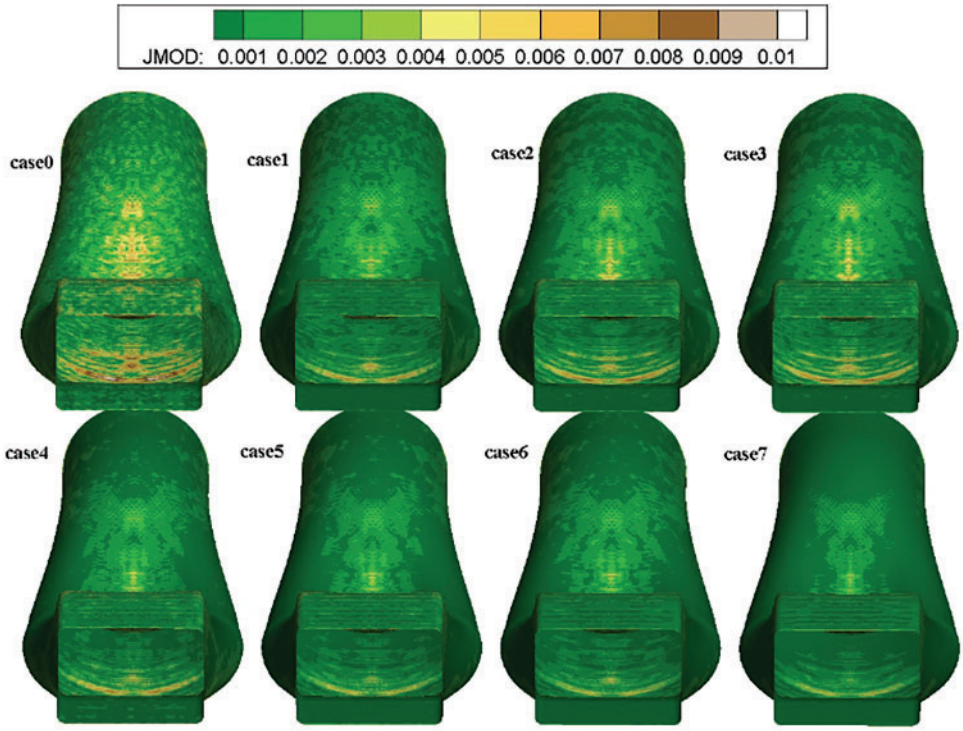

Figure 6: Induced current distribution at $\theta = 20^{\circ}$ in the vertical polarization (unit: mA/m^2)

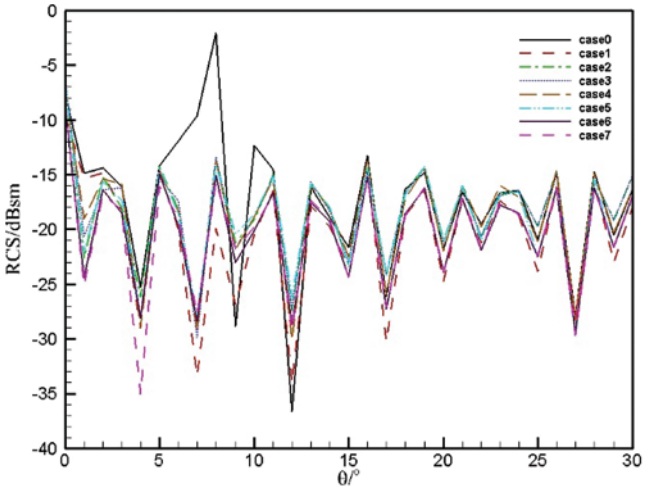

Figure 7: RCS curves of the S-shaped inlet in the horizontal polarization in the yaw plane

Fig. 8 shows the RCS curves of the S-shaped inlet under the vertical polarization in the yaw plane. Within the detection angle range from 0° to 5°, Cases 1 and 4 display RCS angular distribution patterns that are similar to those observed in Case 0. However, the angular distribution patterns of other

coating schemes deviate significantly from that of Case 0. Notably, Case 7 demonstrates a superior RCS reduction effect within the detection angle range from 5° to 10°. Beyond the detection angle of 10°, the RCS angular distribution patterns align closely with that of Case 0. This can be primarily attributed to the direct irradiation of Part 1 by the incident electromagnetic wave.

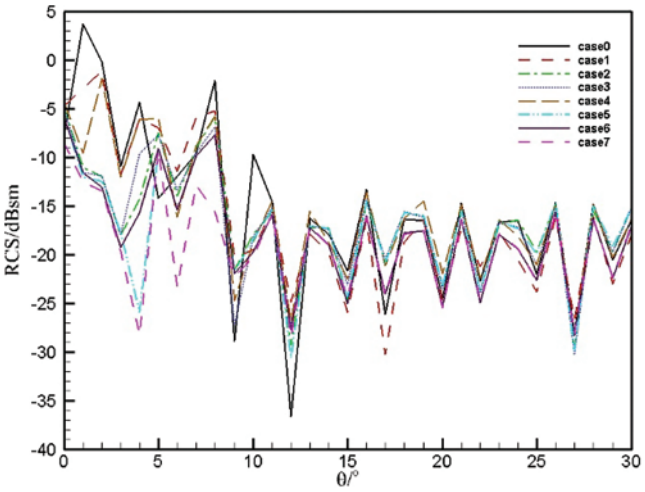

Figure 8: RCS curves of the S-shaped inlet in the vertical polarization in the yaw plane

Fig. 9 shows the induced current distribution in the horizontal polarization in the yaw plane at $\theta = 8^{\circ}$. The figure illustrates two distinct patterns of induced current distribution. In Cases 0, 1, and 4, regions of high-density induced current are observed. Conversely, such high-density regions are absent in other coating schemes. The discrepancy can be primarily attributed to the variations in the coating locations, which subsequently alter the energy of the incident electromagnetic wave.

Fig. 10 shows the induced current distribution in the vertical polarization in the yaw plane at $\theta = 20^{\circ}$. The figure shows that the density distribution of the induced current does not change much at a larger angle of incident detection.

Table 2 shows the average RCS of the different coating schemes in the pitch and yaw planes. The table illustrates that the average RCS of the S-shaped inlet coated with RAM is lower when compared to that without RAM coated. Furthermore, RAM demonstrates a more effective RCS reduction in horizontal polarization than in vertical polarization, across both pitch and yaw planes. The average RCS is the lowest in Case 7 because the surface is fully coated with RAM. The RCS reduction efficiency of Cases 4–6 surpasses that of Cases 1–3, primarily due to the larger area covered by the coating. In terms of horizontal polarization, Case 6 ranks second in RCS reduction efficiency. Conversely, in vertical polarization, Case 5 holds the second position for RCS reduction efficiency. Notably, in the pitch plane, Case 5 achieves an RCS reduction efficiency exceeding ninety percent compared to Case 7, while utilizing only sixty-five percent of the coating area. These observations underscore the critical role of RAM coating and its placement in optimizing RCS performance.

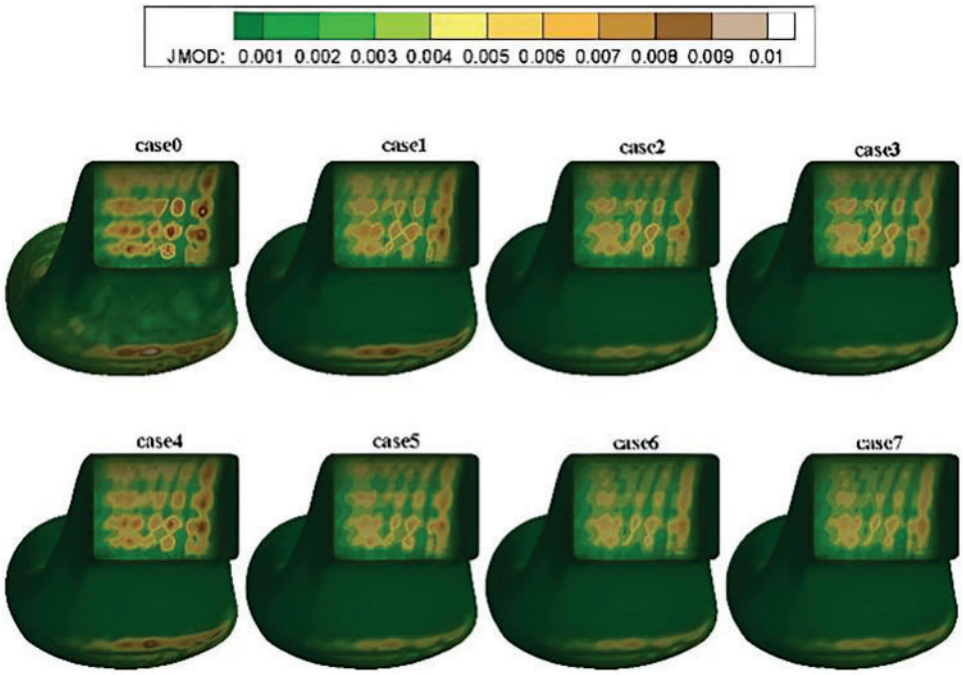

Figure 9: Induced current distribution at in the vertical polarization $\theta = 8^{o}$ (unit: mA/m^2)

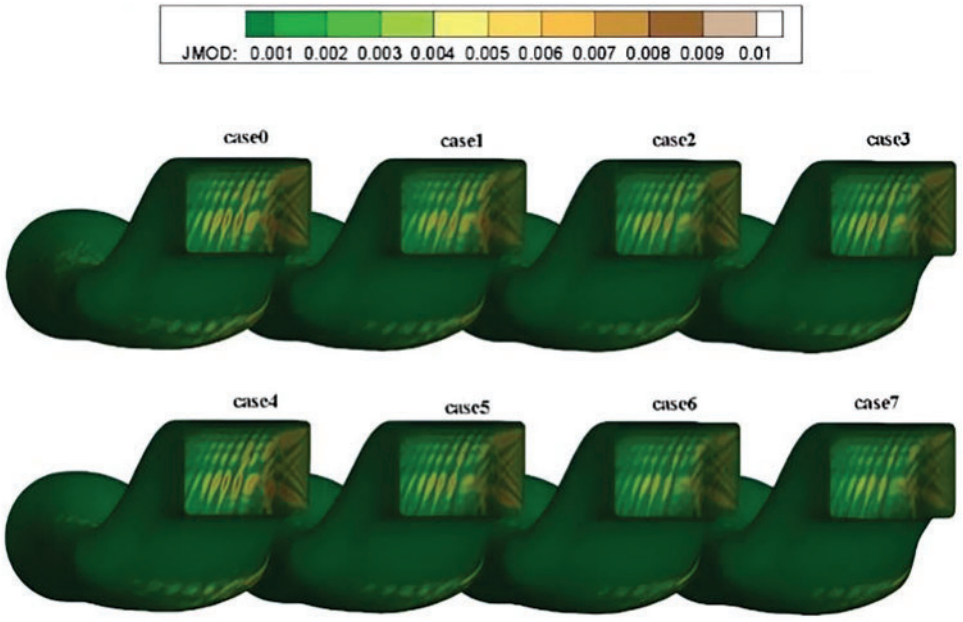

Figure 10: Induced current distribution at $\theta = 20^{o}$ in the vertical polarization (unit: mA/m^2)

Table 2: Average RCS and RCS reduction effect of the different coating schemes (unit: dBsm)

	Pitch plane				Yaw plane			
	Horizontal polarization		Vertical polarization		Horizontal polarization		Vertical polarization	
	Average RCS	RD	Average RCS	RD	Average RCS	RD	Average RCS	RD
Case 0	5.7126		8.2404		−13.0481		−7.6949	
Case 1	−1.4628	−80.84%	3.0993	−69.39%	−17.6377	−65.47%	−10.0784	−42.24%
Case 2	0.2700	−71.44%	5.7387	−43.79%	−16.0934	−50.40%	−13.1184	−71.32%
Case 3	0.2987	−71.25%	5.2804	−49.42%	−15.9308	−48.51%	−13.2039	−71.87%
Case 4	−2.6179	−85.31%	2.4796	−73.46%	−16.2282	−51.92%	−10.9087	−52.29%
Case 5	−3.0312	−86.65%	0.5418	−83.01%	−16.2630	−52.30%	−14.0971	−77.10%
Case 6	−3.3286	−87.53%	0.9023	−81.54%	−17.6667	−65.24%	−14.4135	−78.71%
Case 7	−4.5810	−90.65%	−1.2969	−88.88%	−17.7308	−65.98%	−16.2149	−85.94%

Compared to Case 7, Case 6 utilizes only sixty-one percent of the coating area, yet it achieves an RCS reduction efficiency exceeding ninety percent in the yaw plane. The application of RAM on the surface of the S-shaped inlet results in a more effective RCS reduction in vertical polarization than in horizontal polarization. When contrasted with Case 7, other coating schemes demonstrate an RCS reduction efficiency surpassing seventy percent. In summary, the application of RAM on the surfaces of Parts 3–5 can yield an RCS reduction efficiency of ninety percent. These observations underscore the significant role of RAM coating placement and polarization in optimizing RCS performance.

Table 3 presents the risk characteristic parameter δ of the different coating schemes. The table indicates that Case 7 exhibits the lowest risk value. In the pitch plane, all coating schemes demonstrate larger risk values under horizontal polarization compared to vertical polarization. Case 1 registers the highest risk value under both polarizations. Under horizontal polarization, Case 5 has the second-lowest risk value, whereas under vertical polarization, this position is held by Case 3. In the yaw plane, the risk values for most coating schemes are larger under vertical polarization than under horizontal polarization. The second-lowest risk value is observed in Case 5 under horizontal polarization and in Case 4 under vertical polarization. These observations underscore the influence of polarization and coating schemes on risk values in both pitch and yaw planes. The data underscore the substantial influence of both the coating scheme and the polarization type on risk values. These elements warrant careful consideration during the design and optimization process of the coating scheme for the S-shaped inlet. This information serves as a valuable resource for comprehending and forecasting alterations in the RCS. Furthermore, it facilitates the enhanced design and optimization of the application of RAM.

Table 3: The δ of the different coating schemes

	Pitch plane		Yaw plane	
	Horizontal polarization	Vertical polarization	Horizontal polarization	Vertical polarization
	δ	δ	δ	δ
Case 1	2.00347	1.719703	1.622553	1.04684
Case 2	1.876543	1.15025	1.323877	1.873391
Case 3	1.645117	1.141076	1.120065	1.659432
Case 4	1.425159	1.227197	0.867357	0.873538
Case 5	1.332257	1.276292	0.804121	1.185424
Case 6	1.414741	1.317925	1.054469	1.272184
Case 7	0.9065	0.8888	0.6598	0.8594

4 Conclusions

The electromagnetic scattering characteristics of S-shaped inlets with RAM coated are calculated by the method of the moment with the MLFMM. Firstly, seven coating schemes are designed for the double S-shaped inlet according to the coating area. Secondly, the method of the moment combined with MLFMM is introduced to calculate the forward RCS of the inlet. Finally, the influence of coated schemes on the RCS is discussed with the risk theory. The following conclusions can be drawn:

(1) Coating RAM plays an important role in RCS reduction of the aero engine inlet. All designed coating schemes can reduce the forward RCS of the inlet. The coating scheme Case 7 has the best reduction in RCS by coating RAM on all surfaces.

(2) In comparison with the RCS reduction effect of Case 7, the coating scheme Case 6 can achieve above ninety percent reduction effect while using only approximately sixty percent of RAM. The coating region of Case 6 is distributed on the surface of Parts 3–5 located near the intake of the S-shaped inlet.

(3) The total risk value δ of Case 7 is the lowest in both planes. The risk value δ of Case 4 is the second lowest in both plane

(4) The study can provide technical support for the stealth design of an S-type inlet by using less RAM.

Acknowledgement: None.

Funding Statement: This research is supported by "Key Research and Promotion Special Project (Soft Science) Project of Henan Province, China" (232400410046).

Author Contributions: The authors confirm contribution to the paper as follows: study conception and design: Shuang Liu; data collection: Shuang Liu, Lihai Chen; analysis and interpretation of results: Shuang Liu, Zhiyin Guo. All authors reviewed the results and approved the final version of the manuscript.

Availability of Data and Materials: The data that support the findings of this study are available from the corresponding author, Shuang Liu, upon reasonable request.

Ethics Approval: Not applicable.

Conflicts of Interest: The authors declare that they have no conflicts of interest to report regarding the present study.

References

1. H. X. Huang *et al.*, "Recent progress in subsonic S-shaped inlets," (in Chinese), *J. Propuls Technol.*, vol. 41, no. 12, pp. 2641–2658, Dec. 2020. doi: 10.13675/j.cnki.tjjs.200493.
2. J. H. Sang, *Low-observable technologies of aircraft*. Beijing, China: Aviation Industry Press, 2013.
3. J. J. Zhang, P. L. Huang, and Y. P. Ma, *Stealth principle*. Beijing, China: Beihang University Press, 2018, pp. 143–144.
4. A. Asghar, W. Allan, M. Laviolette, R. Stowe, D. Alexander and G. Ingram, "S-duct diffuser offset-to-length ratio effect on aerodynamic performance of propulsion-system inlet of high speed aircraft," in *ASME Turbo Expo 2018: Turbomachinery Tech. Conf. Exposition*, Oslo, Norway, Jun. 11–15, 2018.
5. G. Mclelland, D. G. Macmanus, P. K. Zachos, D. Gil-Prieto, and M. Migliorini, "Influence of upstream total pressure profiles on S-duct intake flow distortion," *J. Propulsion Power*, vol. 36, no. 3, pp. 346–356, Apr. 2020. doi: 10.2514/1.B37554.
6. M. Migliorini, P. Zachos, and D. Macmanus, "The impact of inlet boundary layer thickness on the unsteady aerodynamics of S-duct intakes," in *AIAA Propul. Energ. 2019 Forum*, Indianapolis, IN, USA, Aug. 19–22, 2019.
7. L. Ning, H. J. Tan, and S. Sun, "Effects of boundary layer ingestion on flow characteristics of an s-shaped inlet," (in Chinese), *J. Propulsion Technol.*, vol. 38, no. 2, pp. 266–273, Jan. 2017. doi: 10.13675/j.cnki.tjjs.2017.02.004.
8. G. X. Song, J. Li, M. X. Tang, Y. Wu, and Y. H. Luo, "Experimental simulation methodology and spatial transition of complex distortion fields in a S-shaped inlet," *Aerosp. Sci. Technol.*, vol. 116, no. 6, Jun. 2021, Art. no. 16855. doi: 10.1016/j.ast.2021.106855.
9. D. Gil-Prieto, P. K. Zachos, D. G. Macmanus, and G. Mclelland, "Unsteady characteristics of S-duct intake flow distortion," *Aerosp. Sci. & Technol.*, vol. 84, no. 6, pp. 938–952, Nov. 2019. doi: 10.1016/j.ast.2018.10.020.
10. W. Gan and X. Zhang, "Design optimization of a three-dimensional diffusing S-duct using a modified SST turbulent model," *Aerosp. Sci. Technol.*, vol. 63, no. 4, pp. 63–72, Jan. 2017. doi: 10.1016/j.ast.2016.12.016.
11. L. Shi and R. W. Guo, "Electromagnetic scattering characteristics of serpentine inlet," *Acta Aeronautica Et Astronautica Sinica*, vol. 28, no. 6, pp. 1296–1301, Nov. 2007. doi: 10.3321/j.issn:1000-6893.2007.06.003.
12. L. Zhang, Z. Zhou, and X. P. Xu, "Area and centerline distribution on stealth design of s-shaped inlet," *J. Syst. Simul.*, vol. 30, no. 8, pp. 2999–3006, Aug. 2018. doi: 10.16182/j.issn1004731x.joss.201808022.
13. L. Wang, Y. C. Zhong, and K. Y. Zhang, "Electromagnetic scattering study for metal/dielectic coated inlet diffuser," *Acta Phys. Sin.*, vol. 61, no. 23, pp. 193–201, Nov. 2012. doi: 10.7498/aps.61.234101.
14. X. Gao, Y. Q. Shi, Q. Z. Yang, and L. H. Chen, "Electromagnetic scattering characteristics of double s-shape exhaust nozzle with different coating medium parts," *Acta Phys. Sin.*, vol. 64, no. 2, pp. 106–115, Dec. 2015. doi: 10.7498/aps.64.024103.
15. Y. B. He, Q. Z. Yang, and X. Gao, "Comprehensive optimization design of aerodynamic and electromagnetic scattering characteristics of serpentine nozzle," *Chin. J. Aeronaut.*, vol. 34, no. 3, pp. 118–128, Jan. 2021. doi: 10.1016/j.cja.2020.10.010.

16. Z. Zhou and J. Huang, "Mixed design of radar/infrared stealth for advanced fighter intake and exhaust system," *Aerosp. Sci. Technol.*, vol. 110, no. 4, Jan. 2021, Art. no. 106490. doi: 10.1016/j.ast.2021.106490.
17. M. Li, J. Q. Bai, X. X. Meng, Q. Liu, and B. Chen, "A gradient-based aero-stealth optimization design method for flying wing aircraft," *Aerosp. Sci. Technol.*, vol. 92, no. 9, pp. 156–169, Jun. 2019. doi: 10.1016/j.ast.2019.05.067.
18. X. L. Chen, L. C. Lu, H. H. Ji, C. Q. Gu, F. Gao and X. J. Shi, "Accurate and efficient simulation method and experimental verification of monostatic RCS for aeroengine exhaust systems," *Acta Aeronautica Et Astronautica Sinica*, vol. 44, no. 12, Jun. 2023, Art. no. 327676. doi: 10.7527/S1000-6893.2022.27676.
19. L. Zhu, "Research on modeling of electromagnetic scattering and radiation characteristics of complex targets based on high-order method of moment," M.S. thesis, Electronic and Communication Engineering, Southwest Univ. of Science and Technology, Chongqing, China, 2021. doi: 10.27415/d.cnki.gxngc.2021.000126.
20. Q. M. Cai, "Research on higher order MoM and fast algorithms for electromagnetic scattering and radiation from metallic and dielectric targets," Ph.D. thesis, Electromagnetic Field and Microwave Technology, Univ. of Electronic Science and Technology, Chengdu, China, 2017.
21. J. Guo, "The study of the theories and the methods of engineering project risk management," M.S. thesis, Management Science and Engineering, Wuhan Univ., Wuhan, China, 2005.